Non-linear resonance modeling and system design improvements for underactuated flapping-wing vehicles*

Noah T. Jafferis[1], Moritz A. Graule[2] and Robert J. Wood[1]

Abstract— Insect-scale flying robots are currently unable to carry the power source and sensor suite required for autonomous operation. To overcome this challenge, we developed and experimentally verified a non-linear damping model of actuation-limited flapping-wing vehicles with passively rotating wing hinges. In agreement with studies on the wing dynamics of honey bees, we found that the optimal angle of the passive wing hinge in mid-stroke is about $70\,^\circ$ rather than $45-50\,^\circ$ as previously assumed. We further identified a narrow actuation force window in which the occurrence of a sharp resonance can be used to achieve both higher lift and efficiency. The findings from our model informed design changes to the Harvard Dual-Actuator Robobee, which resulted in a 130% increase in mean lift from ~140 mg to 320 mg (with a vehicle mass increase of only $5-8\%$), along with a corresponding expected payload increase of $330-470\%$ (30 − 40 mg to 170 mg). The power consumption only increased by ~55%, making the new prototype 50% more efficient at lift production. Our model provides a greater understanding of the dynamics of this complex system, and the resulting lift and efficiency improvements are expected to bring insect-scale flying robots closer to autonomy.

I. INTRODUCTION

Real insects can have a lift-to-mass ratio of ~1.8 (e.g. honey bees – see [1]), where the mass includes all of the necessary components for flight, power, and control. In contrast, while existing flapping-wing vehicles at the scale of small birds (e.g. [2], [3]) have sufficient lift to carry these components (although battery life is limited to several minutes), vehicles at the insect scale have only achieved lift-to-mass ratios of ~1.75 when not including power, sensors, or control ([4], [5]), and ~1.2 with a payload sufficient for sensors and control, but not power [6]. Hence it is clear that we need to increase both the lift-to-actuator mass ratio and the lift-to-power efficiency if such devices are to become practical. Towards this end, we propose that non-linear modeling of the system behavior is important to identify more efficient operating conditions and system designs that might otherwise be missed. Previous work has sought to

approximate the drag felt by the actuation source as a linear function of speed, even if the dynamics of the passive wing rotation are non-linear (e.g. [7], [8]), which limits their ability to be extended to a wide range of operating conditions. In addition, we incorporate performance improvements in actuator fabrication [9] and wing shape [6].

II. DYNAMIC MODEL AND EXPERIMENTAL INVESTIGATION OF INSECT-SCALE WING FLAPPING

A. Model Overview

In this work, we consider flapping-wing vehicles in which the stroke angle (ϕ; see figure 1) is actively controlled – that is, the input to the system is an applied time-varying force which controls the stroke angle through the system dynamics. The angle of attack of the wing is not controlled directly, but instead varies passively due to aerodynamic and inertial torques as well as a restoring torque provided by a passive wing hinge. In our analysis, we refer to the wing hinge angle, ψ, which is $90\,^\circ$ minus the angle of attack, since this is zero in the neutral position of the wing hinge (i.e. perpendicular to the flapping direction; see figure 1). When analyzing the dynamics of such a system, we propose that previously used linear approximations to the wing drag felt by the actuator as a function of speed (e.g. [7]) are not sufficient to explain the resonance behavior in general. This is due to the fact that the passive rotation of the wing results in a highly non-linear drag force [10], which is expected to result in a greatly reduced drag coefficient as the wing passively rotates to greater wing hinge angles ψ. Figure 2 illustrates this effect by plotting the normalized amplitude versus frequency of
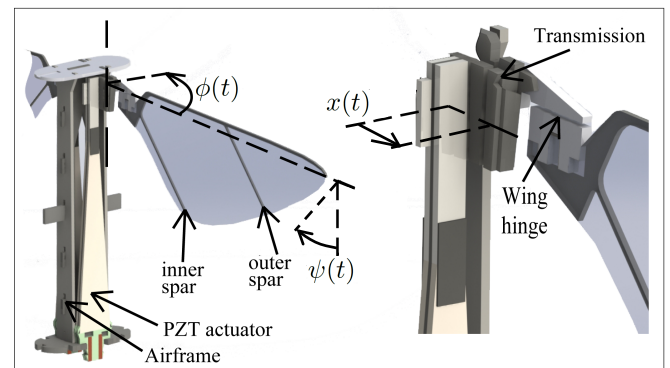
Fig. 1. System diagram and naming conventions. $\psi(t)$ is the wing hinge angle, $\phi(t)$ is the stroke angle, and $x(t)$ is the displacement of the actuator tip.
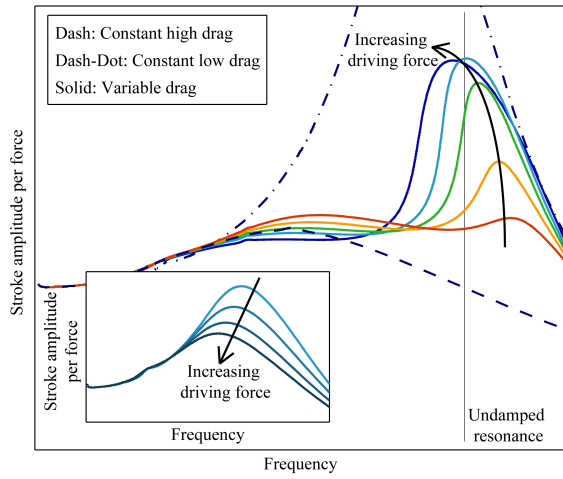
Fig. 2. Amplitude per force frequency response plot illustrating the effect of a harmonic oscillator transitioning from a state of high drag to a state of low drag. Inset shows the variation in the frequency response with driving force amplitude for a quadratic-damping harmonic oscillator.

Fig. 3. Instantaneous lift (blue: $1.8\sin(2\psi)$) and drag (green: $1.9 + 1.5\cos(2\psi)$) coefficients and lift-to-drag ratio (red) as a function of hinge angle.

a harmonic oscillator with two different drag coefficients, one typical of the drag when $\psi = 0$, and the other for $\psi = 75\,^\circ$. Since in the physical system the wing is allowed to passively rotate, we expect the amplitude to transition from the case of high drag to the case of low drag, as illustrated in figure 2. To contrast this non-linear resonance with the resonance behavior of a fixed-drag system, we consider three systems (all driven with a sinusoidal input force) whose normalized frequency response (vibration amplitude per input force amplitude) are plotted in figure 2 for several input force amplitudes: (i) a linear harmonic oscillator (not plotted), (ii) a quadratic-damping harmonic oscillator (inset), and (iii) a "passive-rotation" quadratic-damping harmonic oscillator. For (i), the normalized frequency response is independent of the magnitude of the input force. For (ii), the increased damping coefficient at higher speeds results in a reduction of the resonance frequency and a reduction in the peak normalized amplitude as the force is increased. For (iii), which is the scenario in the actual vehicle, the situation is more complex – three regimes emerge: (a) for low force amplitudes, the wing never reaches high enough speeds to rotate the hinge sufficiently for drag reduction, and the frequency response behaves as in (ii), with a high drag coefficient. (b) For high force amplitudes, the necessary speed is reached well before the un-damped resonance, and the frequency response approaches that of (ii) but with a lower drag coefficient. (c) Most interestingly, for a relatively narrow range of medium forces, the necessary speed is reached well past the high-damping resonance frequency, but near or even slightly past the un-damped resonance frequency (indicated by a vertical line in figure 2). In this case, the frequency response shows an initial broad peak corresponding to the highly damped resonance, followed by a sharp peak as the drag coefficient drops rapidly. As in (ii), this resonance frequency decreases with increasing force, but unlike in (ii), the normalized amplitude peak actually
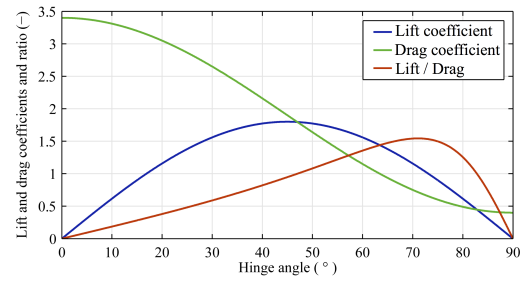
increases with increasing force. This can be understood as follows: the resonance frequency decreases with increasing force for the same reason as in (ii), but in this regime, the resonance frequency at low force is actually higher than the un-damped resonance frequency. This means that higher driving forces bring the resonance frequency closer to the un-damped resonance frequency, which results in a higher relative amplitude peak. This transitional force regime is interesting because it is expected to provide considerably better efficiency (defined as the lift to input power ratio) – that is, the resonances are much sharper and the lift-to-drag ratio is greater. As we will see later (figure 4), the onset of the steep amplitude rise occurs when the maximum hinge angle (ψ_m) is around $50\,^\circ$, which means that to take advantage of this behavior we must allow ψ_m to be greater than this value, contrary to the previous goal of $45-50\,^\circ$. This follows directly from the standard lift and drag expressions as given by [10]: even though instantaneous lift is maximized at $45\,^\circ$, and mean lift (for ideal-phase sinusoidal flapping) when the max hinge angle is $51\,^\circ$ for a fixed frequency (f) and stroke angle amplitude (ϕ_0), the instantaneous lift-to-drag ratio is maximized at $\sim 70\,^\circ$ (depending on the exact lift and drag parameters – an example plot shown in figure 3 uses the same lift and drag coefficients as in [10]). Therefore, since the actuator feels the drag force, the stroke angle amplitude (ϕ_0) is expected to increase as the maximum hinge angle (ψ_m) increases from $45\,^\circ$ to $70\,^\circ$. This more than compensates for the reduced instantaneous lift, resulting in both higher lift and higher efficiency, provided that the phase between the stroke angle ($\phi(t)$) and wing hinge angle ($\psi(t)$) is maintained near $90\,^\circ$. This analysis agrees well with studies of real insect flapping; for example in [11], honeybees were observed to use $\psi_m \approx 60 - 70\,^\circ$. Further, to put this in perspective for flapping-wing vehicles in general, we note that several key features of our analysis, such as higher efficiency operation at $70\,^\circ$ wing hinge angle, are independent of the actuation mechanism.

B. Model in Detail

The detailed model is comprised of a coupled set of differential equations, which describe the actuator (1) and wing hinge angle (2) dynamics. The first of these equations looks like a standard harmonic oscillator describing the

$$m_e x'' + Kx + (C_A + C_B \cos 2\psi)|x'|x' = F_{act} \tag{1}$$

$$I_{xx}\psi'' + \kappa_{wh}\psi + C_C|\psi'|\psi' = C_D x'|x'| + I_{xz}Tx'' \cos\psi + 0.5 I_{xx}(Tx')^2 \sin 2\psi \tag{2}$$

$$K_{act} = p_4 p_5 \frac{w_n G(E_e t_{pzt}(1.5 t_{cf}^2 + 3 t_{cf} t_{pzt} + 2 t_{pzt}^2) + E_{cf} t_{cf}^3/4)}{l_{pzt}^3(1 + 2l_r)} \tag{3}$$

$$F_{1,2} = p_3 \frac{3\,\mathcal{E}_{1,2}\,G\,w_n t_{pzt}(t_{pzt} + t_{cf})(1 + a_2\,\epsilon_{1,2})(f_{31,min} + (f_{31,max}(1 - a_4\,\mathcal{E}_{1,2}) - f_{31,min})e^{a_3\,(\mathcal{E}_{1,2} - \mathcal{E}_0)})}{4 l_{pzt}(1 + e^{a_3(\mathcal{E}_{1,2} - \mathcal{E}_0)})} \tag{6}$$

$$C_D = 0.5\rho A_w W_{cp2}\hat{r}_2^2 T^2 R^2((b_1 + b_2 \cos 2\psi)\cos\psi + b_L \sin 2\psi \sin\psi) \tag{10}$$

---

motion of the actuator tip ($x(t)$), except that the drag is dependent on the wing hinge angle ($\psi(t)$) and varies with velocity squared. Equation (2) includes the terms described in [8] – in order, these are: inertia about the wing hinge axis, stiffness of the wing hinge, rotational damping, rotational torque generated by the lift and drag forces resulting from the time-varying stroke angle ($\phi(t) = x(t)T$, where T is the transmission ratio), and the last two terms give the wing-hinge rotational torque produced by the inertia of the wing about the stroke axis. The effective mass felt by the actuator is $m_e = (I_{zz} + I_{am})T^2$, where I_{zz} and I_{am} are the inertias of the wing and the added-mass of the air surrounding the wing about the stroke angle axis (z). The stiffness felt by the actuator tip is given by $K = K_{act} + T^2\kappa_t$, where K_{act} is the actuator stiffness and κ_t is the transmission stiffness. As derived from [9], K_{act} is given by the strain-dependent expressions (3) and (4), where p_4 is a fitting coefficient to account for an imperfect attachment between the actuator and the airframe, p_5 is set to 0.8 to bring the predicted free deflection of the actuator closer to its measured values (in [9], the actuator deflections are slightly under-predicted), w_n is the mean width of the actuator, G is a gain factor (defined in [9]) determined by the shape of the actuator, t_{pzt} is the thickness of each PZT plate in the actuator, t_{cf} is the thickness of the actuator's central carbon fiber layer, E_{cf} is the modulus of the carbon fiber, l_{pzt} is the length of the active portion of the actuator, l_r is the ratio of the length of the actuator's rigid extension to the length of the PZT, E_{min} and E_{max} are the minimum and maximum moduli of the PZT under varying strain, ϵ_0 is the strain at which the modulus transitions from E_{min} to E_{max}, a_1 represents the steepness of this transition, and $\epsilon = -|\epsilon_1|$ is the magnitude of the compressive strain in the actuator.

$$E_e = E_{min} - \frac{E_{max} - E_{min}}{2a_1\,\epsilon} \ln\left[\frac{1 + e^{a_1(\epsilon_0 - \epsilon)}}{1 + e^{a_1\,\epsilon_0}}\right] \tag{4}$$

The compressive strain in each of the two PZT plates is

$$\epsilon_{1,2} = \mp\frac{(t_{pzt} + t_{cf})x}{l_{pzt}^2(1 + 2l_r)}. \tag{5}$$

The driving force provided by the actuator (derived from [9]) is given by the difference in forces provided by each PZT plate ($F_{act} = F_1 - F_2$). F_1 and F_2 are computed according to (6), where p_3 is a fitting coefficient to account

for an imperfect attachment between the actuator and the air frame, a_2 represents a slight linear increase in the force with increasing compressive strain, $f_{31,min}$ and $f_{31,max}$ are the minimum and maximum values of the piezoelectric stress per field coupling coefficient in the field dependency of this piezoelectric coupling coefficient, $\mathcal{E}_0$ is the field at which this transition occurs, a_3 represents the steepness of this transition and a_4 represents a slight linear decline in the piezo stress coefficient at high fields. The time-varying electric field applied to each of the PZT plates,

$$\mathcal{E}_{1,2}(t) = (0.5 V_{pp}/t_{pzt})(1 \mp \sin[2\pi(1 + 15\,t/2)\,t]) \tag{7}$$

(with applied peak-to-peak voltage V_{pp}), is set to be a sinusoidal frequency sweep beginning at $1\,\mathrm{Hz}$ at time $t_0 = 0$ and increasing in frequency by $15\,\mathrm{Hz}$ per second. Lastly, $C_{A,B}$ are the standard drag coefficients given by

$$C_{A,B} = 0.5\rho A_w R_{cp}\hat{r}_2^2 T^3 R^2 b_{1,2}, \tag{8}$$

where ρ is the density of air, A_w is the wing area, R_{cp} is the radial center of pressure, $\hat{r}_2$ is the standard wing-shape parameter, R is the distance from the transmission flexure to the wing tip, $b_{1,2} = (b_{max} \pm b_{min})/2$, and b_{max} and b_{min} give the drag at $\psi = 90\,^\circ$ and $0\,^\circ$ respectively. Moving on to (2), I_{xx} is the inertia of the wing about the wing hinge axis (x), I_{xy} is the coupling inertia between the x and y axes, κ_{wh} is the stiffness of the passive wing hinge, and the damping coefficient for the wing hinge rotation is given by

$$C_C = 0.5\rho A_w W_{cp1}\hat{w}_2^2 W^2 b_{max}. \tag{9}$$

W_{cp1}, $\hat{w}_2$, and W are analogous to R_{cp}, $\hat{r}_2$, and R, but for rotation about x instead of z. In the coefficient for the lift and drag torque term (10), the effective chord-wise center of pressure as a function of wing hinge angle is given (as in [12] and [8]) by

$$W_{cp2} = W_{av}\left(p_{min} + (p_{max} - p_{min})\left|1 - \psi\frac{2}{\pi}\right|\right) \tag{11}$$

where $W_{av} = A_w/R$ is the mean width of the wing, and p_{min} and p_{max} are fitting parameters in our case.

C. Experimental Validation and Parameter Fitting

We built and characterized a test device to experimentally validate this non-linear resonance and tune parameter values
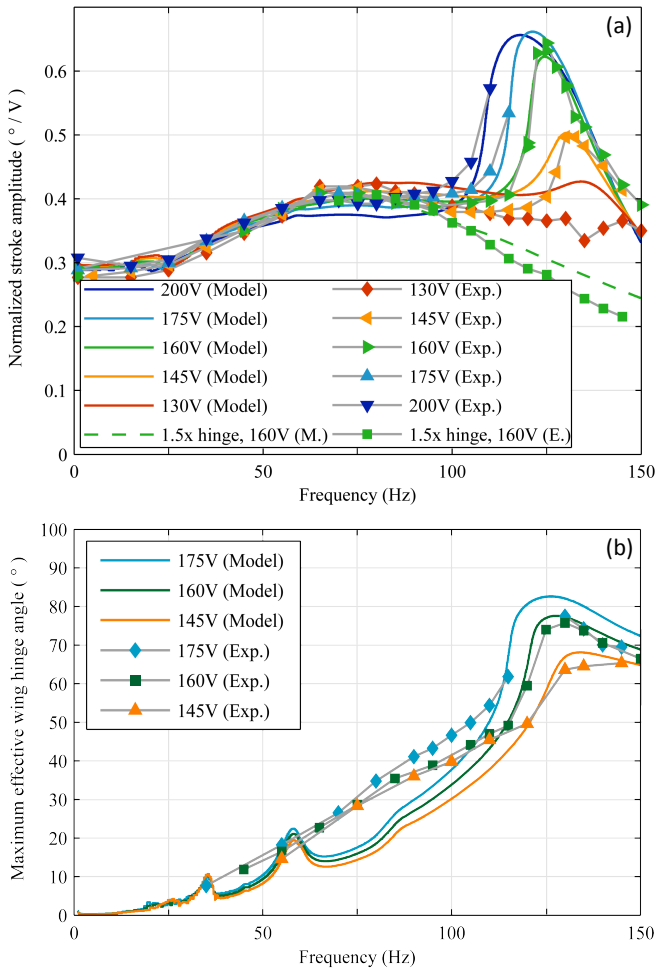
Fig. 4. Data and model fit (parameter values given in table 1) for (a) peak-to-peak stroke angle ($2\phi_0$) normalized by peak-to-peak applied voltage (V_{pp}), and (b) maximum wing hinge angle (ψ_m) plotted as a function of frequency for several applied voltages (listed by the peak-to-peak voltage). In (b), the data shown is the average of the measured inner and outer wing spars angles.

does not provide enough time for the airframe to move significantly. Accordingly, the slow-motion videos of the Harvard Dual-Actuator Bee [4] show that the body's motion during stable hovering is small and slow compared to the wing motion.

The values used for all parameters in the model equations are shown in table I – in cases where the value used differs from an expected value, the value is shown as a fitting pre-factor multiplied by the expected value. The parameters $f_{31,min}$, $f_{31,max}$, $a_{1,2,3,4}$, $\mathcal{E}_0$, E_{min}, E_{max}, ϵ_0, and E_{cf} are as used in the actuator model in [9]. t_{pzt}, t_{cf}, l_{pzt}, w_n, l_r, and w_r are as measured for the actuator dimensions. Expected values for the wing inertia parameters I_{zz}, I_{xx}, and I_{xz} are determined from a SolidWorks model – for the fit, I_{zz} and I_{xx} are very close to these values, but I_{xz} is only 29% of the expected value. The inertia of the added air mass I_{am} is used as a fitting parameter (a rough estimate for this is the inertia of a cylinder of air with length R and diameter W_{av} – the value we use is approximately twice this estimate). The parameters relating to wing shape (R, $\hat{r}_2$, W, $\hat{w}_2$, and A_w) are as calculated in SolidWorks. The aerodynamic lift and drag coefficients are given as fitting pre-factors multiplied by the values measured in [10] for Drosophila wings. The rotational center of pressures, R_{cp} and W_{cp1}, are given as fitting parameters multiplied by $\hat{r}_2R$ and $\hat{w}_2W$, respectively. Our values for actuator force and stiffness are ~$20-30\%$ lower (scaled by p_3 and p_4 respectively) than expected due to non-ideal base attachment – that is, with the improved actuators [9] bending no longer occurs at the interface between the PZT and the actuator base, but is now seen to occur at the attachment between the actuator base and the robot airframe (i.e. mechanical ground). This bending is less than that typically found in the dual-actuator bee, but there is still potential for further improvement. To determine the transmission stiffness in the actuator coordinate frame, K_t, we first look at the ideal value given by $T^2\kappa_t$, where κ_t is calculated from simple beam bending theory. As the value achieved in the vehicle may differ from this due to non-idealities such as misalignments, we perform a simple measurement of the actuator deflection at DC both before and after the transmission is connected – this gives us the effective transmission stiffness as a fraction of the effective actuator stiffness (at the strain condition in which the measurement is taken). For this vehicle, we find that these are equal (i.e. $K_t \approx p_4K_{act}$ when measured at a tip deflection of about $480\,\mu m$ peak-to-peak). As can be seen in figure 4a, the model now matches the stroke angle amplitude data quite well over a range of different force inputs, with both showing the non-linear resonance behavior described in section II-A. Figure 4b shows that the maximum wing hinge angle data match the model well near the main resonance frequency (where we expect the vehicle to be operating), but the model predicts small resonance peaks at about 60 Hz and 35 Hz which are not observed in the data. While the data is not finely spaced enough to rule out the presence of small peaks, this likely indicates that there is more rotational damping at low speeds then expected

in the dynamics equations. This vehicle is the same as the Harvard Dual-Actuator Robobee [5] except for the use of actuators fabricated according to the improved methods described in [9]. Figure 4 shows $2\phi_0/V_{pp}$, and ψ_m as functions of frequency for several input voltages, along with the model results. The measurements are obtained by recording the flapping of the wing with a high-speed camera looking in a direction perpendicular to the plane of the wing stroke motion. This allows $\phi(t)$ to be measured directly by tracking the leading edge of the wing, and $\psi(t)$ can be calculated from the projected angle between the leading edge and the wing spars. Both spars are tracked, as some twisting of the wing occurs - the values shown are the average of the inner and outer spar angles. While all of the flapping dynamics experiments in this work are performed with the airframe fixed in place, we do not expect this to result in significantly different behavior than that in hovering flight. This is because the inertia of the airframe is much greater than that of the wings, and the high flapping frequency

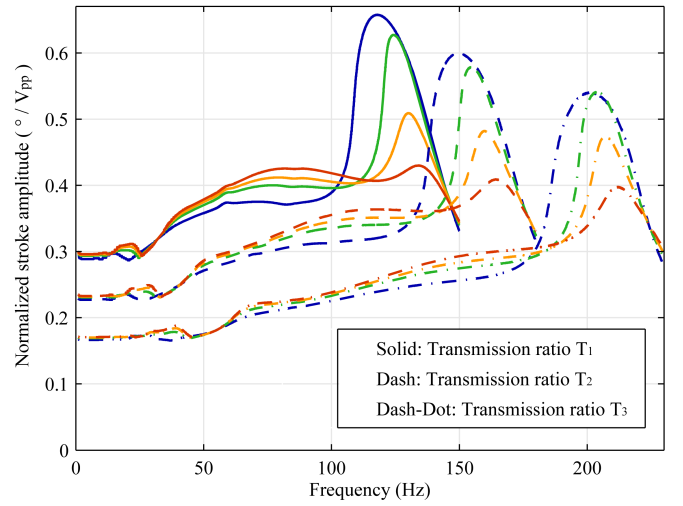| Symbol	Value	Unit
$f_{31,min}$	14	N/Vm
$f_{31,max}$	29	N/Vm
a_1	8000	
a_2	-230	
a_3	10	μm/V
a_4	69	nm/V
$\mathcal{E}_0$	0.4	V/μm
E_{min}	38.5	GPa
E_{max}	81	GPa
ϵ_0	-0.047	%
E_{cf}	340	GPa
t_{pzt}	135	μm
t_{cf}	50	μm
l_{pzt}	9	mm
w_n	1.125	mm
l_r	0.25	
w_r	1.556	
p_5	0.8	
p_4	0.79	
p_3	0.7	
C_{act}	10.1	nF
T	3333	rad/m
K_t	197.7	N/m
I_{zz}	51.1	mg mm^2
I_{am}	10.22	mg mm^2
I_{xx}	0.95×1.29	mg mm^2
I_{xz}	0.29×2.8	mg mm^2
R	17	mm
A_w	54.59	mm^2
$\hat{r}_2$	0.564	
W	4.5	mm
$\hat{w}_2$	0.43	
b_{max}	1.25×3.4	
b_{min}	0.39×0.4	
b_L	1.8	
R_{cp}	1.42×9.56	mm
W_{cp1}	0.39×1.93	mm
p_{min}	0.132	
p_{max}	0.151	
κ_{wh}	0.985×1.52	μNm/rad

Fig. 5. Normalized frequency response plots from the model for three transmission ratios (and the corresponding values of κ_T and κ_{wh}). T_1 represents the initial values of T, κ_T, and κ_{wh}, T_2 represents $0.8T$, $0.8^{-2.14}\kappa_T$, $0.8^{-1.47}\kappa_{wh}$, and T_3 represents $0.6T$, $0.6^{-2.14}\kappa_T$, $0.6^{-1.47}\kappa_{wh}$

from the model. Additionally, twisting of the wing was not accounted for in our model, which may contribute to the discrepancy in the 60-100 Hz range. Finally, we note that, with the lower actuator force and stiffness in the original dual-actuator bee (which did not use the fabrication method described in [9]), many of those vehicles did not enter into the force window necessary to achieve the sharp resonances, or if they did it required higher voltages to get there.

III. IMPLICATIONS FOR IMPROVED VEHICLE DESIGN

A. Model-Informed Design Principles

Now that we have at hand a reasonable model for the non-linear resonance behavior of our flapping-wing robot, we consider how we can use this model to inform design changes for an improved vehicle. First, as noted above, we can choose κ_{wh} to achieve $\phi_m \approx 70\,^\circ$ instead of $45-50\,^\circ$ in order to achieve greater efficiency (and thus greater lift for an actuation-limited vehicle). Beyond that, there are a large number of system properties that could be varied – these can be roughly split into three categories of parameters: actuation, wings, and the coupling between these (transmission). In this paper we keep the actuator size fixed and consider primarily the transmission, although some changes to the wings will be noted later. The main transmission parameters are the transmission ratio and stiffness (we ignore its inertia and damping, as these are typically small compared to that of the wing). Considering first the transmission ratio, note that pervious work [7] has suggested that reducing it somewhat results in greater lift, while further reduction leads to declining lift. However, this analysis assumed that the operation amplitude was the same as the DC amplitude, and kept the transmission bending stiffness fixed. Here we use our model of the dynamics to predict the resonance amplitude as well as frequency, and also allow the transmission stiffness and wing hinge stiffness to be changed. With this analysis, we will see that decreasing T increases the resonance frequency faster than decreasing the amplitude at resonance, at least until the effective mass felt by the actuator becomes dominated by the actuator mass rather than the wing inertia. For our case, the effective actuator mass can be estimated from the unloaded resonance (f_{res} is about $900\,\mathrm{Hz}$) as $K_{act}/(2\pi f_{res})^2 \approx 7\,\mathrm{mg}$ (this is smaller than the actual actuator mass of $25\,\mathrm{mg}$, as expected), while the effective mass due to the wing inertia is $\sim 570\,\mathrm{mg}$ (and with the added mass effect due to the air, $\sim 700\,\mathrm{mg}$). Hence, T would need to be reduced by a factor of $3-4$ for the actuator mass to be even a 10% contribution, so we ignore this contribution in our analysis. In more detail, we see that the resonance frequency increases roughly according to $1/T$ at the same applied voltage amplitude, provided that the transmission stiffness and wing hinge stiffness are

increased in such a way as to ensure that a similar family of curves occurs (i.e. the relation between the resonance curves for the various applied voltages). If these parameters are scaled properly, the amplitude at resonance decreases slower than the resonance frequency increases, and the square of the resulting speed increase can be matched with the increase in wing hinge stiffness, which to first order is expected to result in similar wing hinge rotation. While the exact required scaling of κ_T and κ_{wh} is not derived in this paper, due to uncertainty in the exact parameter values, we note that for the fit described in section II-C, an approximate match can be found by scaling κ_T with $1/T^{2.14}$ (note that this is only slightly more than the $1/T^2$ scaling required to keep the transmission stiffness constant in the actuator coordinate frame) and scaling κ_{wh} with $1/T^{1.47}$. Figure 5 shows the result of following these scaling relations for transmission ratio reductions of 20% and 40%. Together this implies that we expect the mean lift force to scale approximately as $1/T^{1.47}$ (since κ_{wh} increases by about the same as $(\phi_0 f)^2$, we can use this as a rough estimate for lift), while the input power (P) only increases as $\sim 1/T$ (since this is the change in frequency for the same voltage). P is defined here as $0.5 C_{act} V pp^2 f$ (where C_{act} is the total capacitance of both actuators), however, given typical boost-converter efficiencies at this scale, the actual power required is expected to be 2-3 times larger in practice. Note that this analysis presumes that the initial configuration before changing T gives us a "desirable" family of frequency response curves, but does not seek to determine what the ideal such picture is (besides noting that the presence of the sharp non-linear resonance peaks is intimately tied to allowing the wing hinge to rotate past about $50\,^\circ$, and is expected to result in greater lift and efficiency). From a system-wide perspective, there may be several tradeoffs involved in determining the ideal such picture, such as maximum lift (utilizing the highest available voltage) vs. maximum efficiency (utilizing lower voltages but reaching close to maximal lift).

Several take-away lessons from the model presented above are as follows: (1) Design for $\psi_{max} \approx 70\,^\circ$ instead of $45 - 50\,^\circ$. (2) Decrease transmission ratio until the actuator mass becomes significant relative to the wing inertia. (3) Increase transmission stiffness with $1/T^{2.14}$ and wing hinge stiffness with $1/T^{1.47}$ to maintain a similar family of frequency response curves. Note that this scaling implies that the actuator/transmission undamped resonance frequency $((K_{act} + K_t)^{0.5}/(I_{zz}^{0.5} T))$ increases faster than the wing hinge undamped resonance frequency $(\kappa_{wh}^{0.5}/I_{xx})$. Therefore, such scaling is likely not sustainable as these frequencies approach one another unless something else about the system, such as wing inertia values, is also changed. (4) For the coupled changes in transmission ratio and stiffness and wing hinge stiffness, we expect an increase in mean lift of about $1/T^{1.47}$, and an efficiency increase of about $1/T^{0.47}$, bearing in mind that these scaling relations may change somewhat with variations in the many other parameters involved in the complete system. We also expect further increases in lift and efficiency from the change in ψ_{max} – for example, the lift-to-drag ratio is about 50% higher at $\psi_{max} = 70\,^\circ$ than at $45 - 50\,^\circ$ in figure 3.

B. Vehicle Redesign

Now that we have a prediction for several vehicle design changes expected to improve performance, we proceed to the actual construction of a test device incorporating these changes. As discussed above, our model indicates that we should reduce the transmission ratio considerably to improve performance; however, this effect is not "free" from a system-wide perspective. This is due to the fact that as the transmission ratio is reduced, the actuator must undergo greater strain to accomplish the same stroke amplitude, and since the actuator is composed of a brittle material its lifetime is expected to drop rapidly as the ultimate failure strain is approached (for example, in [9], a 20% change in failure strain resulted in a 5× change in lifetime). In this perspective, transmission ratio reduction is essentially a trade-off between lift and lifetime. In the original Robobee [4], actuator lifetime was already relatively short, so further reduction was not feasible; however, with the ~30× increase in lifetime at the same tip deflection reported in [9], such a tradeoff is now practical. To maintain a reasonable lifetime, we reduce the transmission ratio by 20% from $3333\,\mathrm{rad/m}$ to $2666\,\mathrm{rad/m}$. The approximate scaling relations suggested by the model would then indicate that we should increase κ_T by $1/0.8^{2.14} = 1.61\times$ and κ_{wh} by $1/0.8^{1.47} = 1.39\times$. This corresponds to the parameters used in figure 5b. Before we proceed to choose our new stiffness values, we note two other changes in the design of our new test vehicle: (1) To make assembly easier, we followed a fabrication design inspired by "BigBee" [6]. This design utilizes a separate transmission for each actuator and replaces the "spherical" joint of the dual-actuator bee's transmission [5] with a parallel geometry that is easier to assemble reproducibly. However, a parallel joint causes increased strain in the transmission flexures and actuator, which would prevent us from reducing the transmission ratio as desired. To alleviate this issue we inserted additional "tabs" between the actuator tip and the transmission that allow some degree of rotation perpendicular to the transmission flexures. (2) Optimization
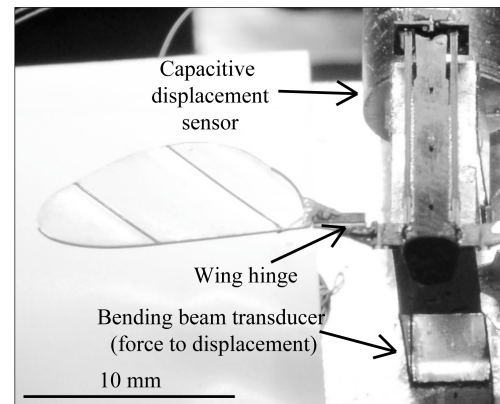

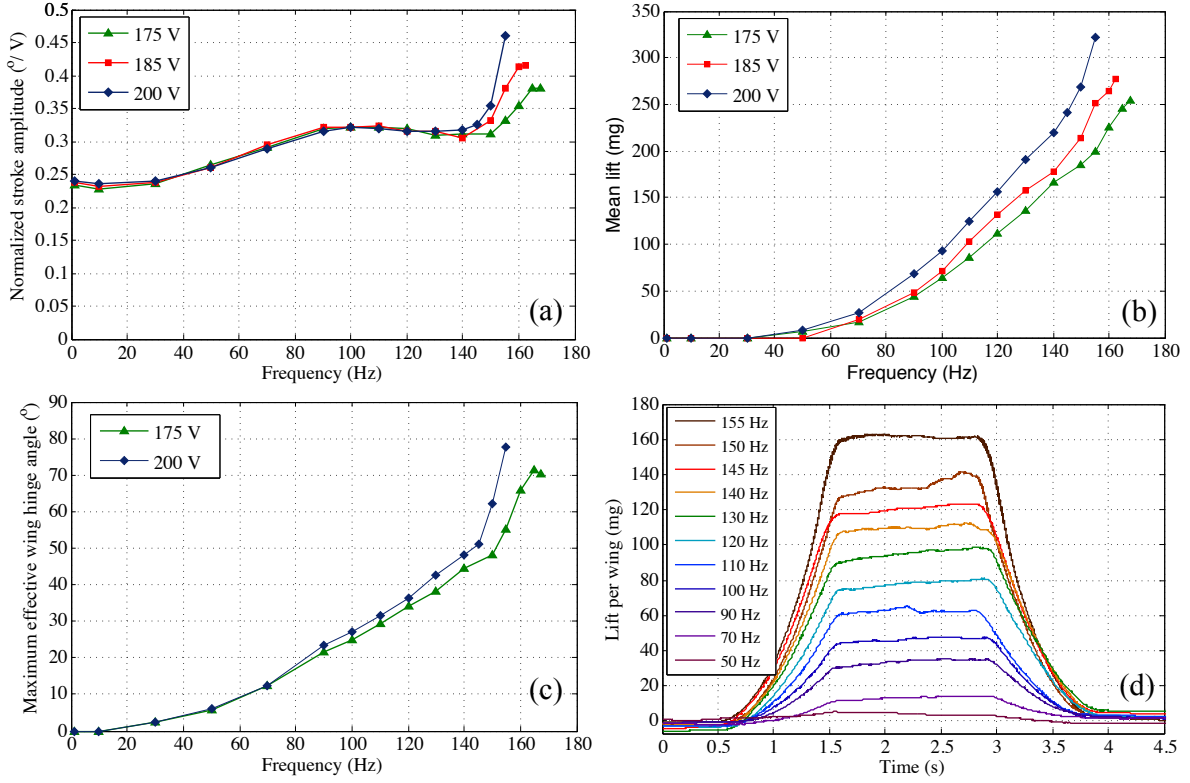Fig. 6. A test vehicle mounted on a capacitive force sensor.

Fig. 7. Characterization results for the improved vehicle. (a) Normalized stroke amplitude. (b) Mean lift versus frequency. (c) Maximum wing hinge angle (average of measurements taken from the inner and outer wing spars) versus frequency. (d) Mean lift per wing shown over the duration of each measurement − the voltage is initially off, then ramps up to $200\,V_{pp}$, stays there for about one second, and then ramps back down to zero.

of wing shape is outside the scope of this work, however, we use wings shaped as in [6] (but with the same area as the dual-actuator bee), due to their higher lift-to-drag ratio as compared to those used in the dual-actuator bee. Returning now to determining the new κ_T, first recall from section II-C that the value calculated from beam bending theory was less than that measured in the robot, with the difference likely due to misalignment during assembly. Given the easier assembly of our new test vehicle, we anticipate this issue to be mostly resolved, and choose κ_T to result directly in the desired stiffness. On the other hand, while this vehicle used a slightly different actuator-to-airframe attachment than in our first test vehicle, some bending at this interface is still present, so for the purposes of this paper we assume that no significant difference in this area is expected. Thus we increase κ_T by $2.6\times$ from $10.8\,\mu Nm/rad$ to $28.2\,\mu Nm/rad$, with measurements indicating that $K_{T,eff}$ is about $215\,N/m$, 8% greater than in our first test vehicle ($198\,N/m$), and close to the desired scaling of $1.61 \times 0.8^2 = 1.03\times$. Finally, we increase κ_{wh} by 50% from 1.52 to $2.29\,\mu Nm/rad$ − somewhat more than that prescribed by the model to partially account for the easier rotation of the new wings. In order to produce this stiffer wing hinge, we simply widen the hinge – this ensures that the strain and off-axis twisting of the wing hinge are not adversely affected. The attachment between the wing and the wing hinge is adjusted to ensure that the position of the wing is not shifted out by this change.

IV. RESULTS

To characterize our new test vehicle, we mount it to a custom-built capacitive force sensor (figure 6) and record the wing flapping with a high-speed camera as for our earlier tests. The resulting scaled wing stroke amplitudes, mean lift, and max wing hinge angle measurements are shown in figure 7a, b, and c, respectively, as a function of frequency. Since only one wing was used in these tests, the reported lift is the measured lift multiplied by two (other tests have shown that the lift measured with two wings is within a few percent of the sum of the lifts from each wing individually). As can be seen (figure 7a), the same sharp resonance in amplitude is seen as in the previous test device, and mean lift (figure 7b) rises to a maximum measured value of $320\,mg$, 130% greater than the $140\,mg$ of the original dual-actuator bee. Figure 7d shows mean lift measurements for each of the one second flapping tests at $200\,V$. At the peak lift, $155\,Hz$, $200\,V$ operating point, we have an input power $P = 0.5 C_{act} V_{pp}^2 f = 31\,mW$, only 55% higher than the $20\,mW$ reported for the dual-actuator bee [4]. This results in a lift-to-power efficiency increase of ~50%. Further, we can estimate the payload that this vehicle can carry (table II) by noting that in [4] and [6], the maximum mass that those vehicles were capable of lifting during hovering flight was about 80% of their maximum lift measurements, due to the need for extra lift to allow for control. Comparing these results to the model, we expected a lift increase of $1/0.8^{1.47} = 1.39\times$

TABLE II

DESIGN AND PERFORMANCE PARAMETERS OF PREVIOUS AND
MODEL-INFORMED INSECT-SCALE FLAPPING WING FLYER

Parameter	Previous [4]	Improved	Remarks
ϵ_f	0.25%	0.32%	see [9]
ϵ_{max}	0.066%	0.079%	
T	3333 rad/m	2666 rad/m	
K_t	198 N/m	215 N/m	effective
G_T	spherical	parallel + tabs	
κ_{wh}	1.52 μNm/rad	2.29 μNm/rad	
M_f	80 mg	87 mg	
$\bar{F}_{L,max}$	140 mg	320 mg	
η	7 mg/mW	10.3 mg/mW	
m_{pl}	30 − 40 mg	170 mg	predicted

Fig. 8.   Complete vehicle.

from the transmission change (and an efficiency increase of $1/0.8^{0.55} = 1.11$), combined with an estimated 50% increase in lift and efficiency from the higher ψ_{max}. All together, this predicts an increase in lift from 140 mg to ~290 mg and about a 66% increase in efficiency. Thus, our results are within ~10% of our predictions (the lift is 10% greater than predicted and the efficiency is 10% lower), indicating that the model can provide useful guidelines for vehicle design. The differences that we do see are likely due to the wing shape change. Note that the resonance frequency is around 160 Hz, which is slightly higher than predicted (see figure 5) – this is likely due to a combination of the new wing shape and the wing hinge being slightly stiffer than that prescribed by the model (section III-B). Finally, we note that given the peak-to-peak stroke angle $2\phi_0$ of $92°$, the maximum strain experienced by the actuator in the peak-lift condition is about what it would have been in the original Robobee at $2\phi_0 = 115°$ – this is $15 − 25\%$ more than the typical operation in that vehicle. Since this strain increase is less than the 28% increase in actuator failure strain (see [9] and table II), it could be feasible to reduce the transmission ratio slightly more in future designs, resulting in even greater lift and efficiency.

V. CONCLUSIONS

We identify and describe nonlinear resonance behavior in passive-rotation flapping-wing systems through both modeling and experimental validation. This behavior occurs only over a relatively narrow range of actuation forces, requiring careful matching of several system parameters to achieve (e.g. actuator force and stiffness, transmission ratio and stiffness, and wing hinge stiffness) and results in higher lift and efficiency. This is primarily due to the greater maximum wing hinge rotation (about $70°$ instead of $45 − 50°$), which is consistent with that found in real insects. The model is shown to be reasonably effective at predicting how to further increase lift through transmission ratio reduction by varying transmission ratio, transmission stiffness, and wing hinge stiffness simultaneously to ensure that the available forces remain within the required window. A new test vehicle is constructed according to these guidelines (design and per-
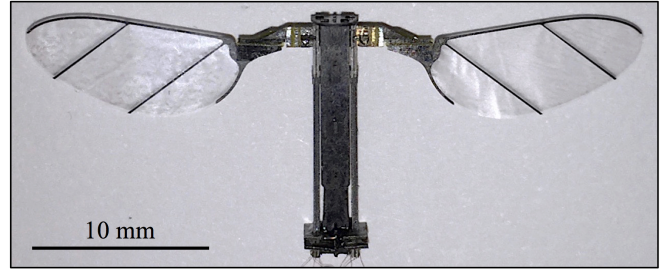
formance parameters are shown in table II and the complete vehicle is shown in figure 8), and is shown to achieve a 130% increase in mean lift, resulting in the lift-to-mass ratio (without power, sensors, or control) increasing from 1.75 to 3.7, and an efficiency increase of 50%, without requiring any change in actuator size or wing area. Based on our measured lift forces, we expect a corresponding expected payload increase of $330 − 470\%$ (30 − 40 mg to 170 mg), which will be utilized in future work on on-board sensing, control, and power.

REFERENCES

[1] E. Feuerbacher, J. H. Fewell, S. P. Roberts, E. F. Smith, and J. F. Harrison, "Effects of load type (pollen or nectar) and load mass on hovering metabolic rate and mechanical power output in the honey bee apis mellifera," *Journal of Experimental Biology*, vol. 206, no. 11, pp. 1855–1865, 2003.

[2] M. Keennon, K. Klingebiel, H. Won, and A. Andriukov, "Development of the nano hummingbird: A tailless flapping wing micro air vehicle," *AIAA Aerospace Sciences Meeting*, pp. 1–24, 2012.

[3] D. Lentink, S. R. Jongerius, and N. L. Bradshaw, "The scalable design of flapping micro-air vehicles inspired by insect flight," *Flying insects and robots*, pp. 185–205, 2010.

[4] K. Y. Ma, P. Chirarattananon, S. B. Fuller, and R. J. Wood, "Controlled flight of a biologically inspired, insect-scale robot," *Science*, vol. 340, no. 6132, pp. 603–607, 2013.

[5] K. Y. Ma, S. M. Felton, and R. J. Wood, "Design, fabrication, and modeling of the split actuator microrobotic bee," *Intelligent Robots and Systems (IROS), 2012 IEEE/RSJ International Conference on*, pp. 1133–1140, 2012.

[6] K. Y. Ma, P. Chirarattananon, and R. J. Wood, "Design and fabrication of an insect-scale flying robot for control autonomy," *to appear in Intelligent Robots and Systems (IROS), 2015 IEEE/RSJ International Conference on*, 2015.

[7] B. M. Finio, N. O. Pérez-Arancibia, and R. J. Wood, "System identification and linear time-invariant modeling of an insect-sized flapping-wing micro air vehicle," *Intelligent Robots and Systems (IROS), 2011 IEEE/RSJ International Conference on*, pp. 1107–1114, 2011.

[8] J. Whitney and R. Wood, "Aeromechanics of passive rotation in flapping flight," *Journal of Fluid Mechanics*, vol. 660, pp. 197–220, 2010.

[9] N. T. Jafferis, M. J. Smith, and R. J. Wood, "Design and manufacturing rules for maximizing the performance of polycrystalline piezoelectric bending actuators," *Smart Materials and Structures*, vol. 24, no. 6, p. 065023, 2015.

[10] M. H. Dickinson, F.-O. Lehmann, and S. P. Sane, "Wing rotation and the aerodynamic basis of insect flight," *Science*, vol. 284, no. 5422, pp. 1954–1960, 1999.

[11] J. T. Vance, D. L. Altshuler, W. B. Dickson, M. H. Dickinson, and S. P. Roberts, "Hovering flight in the honeybee apis mellifera: Kinematic mechanisms for varying aerodynamic forces." *Physiological and biochemical zoology: PBZ*, vol. 87, no. 6, pp. 870–881, 2013.

[12] W. B. Dickson, A. D. Straw, C. Poelma, and M. H. Dickinson, "An integrative model of insect flight control," *Proceedings of the AIAA Aerospace Sciences Meeting and Exhibit, Reno, NV*, 2012.